



# Rational design of high concentration electrolytes and MXene-based sulfur host materials toward high-performance magnesium sulfur batteries

Hao Xu<sup>a,b,c</sup>, Dong Zhu<sup>d,e</sup>, Wen Zhu<sup>a,b,c</sup>, Fengzhan Sun<sup>a,b,c</sup>, Jianxin Zou<sup>a,b,c,\*</sup>, Richard M. Laine<sup>f,\*</sup>, Wenjiang Ding<sup>a,b,c</sup>

<sup>a</sup> National Engineering Research Center of Light Alloy Net Forming, School of Materials Science and Engineering, Shanghai Jiao Tong University, Shanghai 200240, China

<sup>b</sup> State Key Laboratory of Metal Matrix Composites, School of Materials Science and Engineering, Shanghai Jiao Tong University, Shanghai 200240, China

<sup>c</sup> Center of Hydrogen Science, Shanghai Jiao Tong University, Shanghai 200240, China

<sup>d</sup> Computer Network Information Center, Chinese Academy of Science, Beijing 100190, China

<sup>e</sup> University of Chinese Academy of Science, Beijing 100049, China

<sup>f</sup> Department of Materials Science and Engineering, University of Michigan, Ann Arbor, MI 48109-2136, United States

## ARTICLE INFO

### Keywords:

MXene  
Ti<sub>3</sub>C<sub>2</sub>@CoO  
Mg(TFSI)<sub>2</sub>-based electrolytes  
Magnesium sulfur batteries

## ABSTRACT

Rechargeable magnesium sulfur batteries (MSBs) assembled with earth-abundant and safe Mg anodes less prone to form dendrites on surface and sulfur-containing cathodes offer considerable potential for high energy densities. Nevertheless, suitable sulfur host materials and electrolytes are at present key factors that retard commercial introduction. Here, we explore preparation of Ti<sub>3</sub>C<sub>2</sub>@CoO composites as sulfur hosts with high concentration electrolytes consisting of Mg(TFSI)<sub>2</sub> and AlCl<sub>3</sub> in diglyme as new types of MSBs. Density functional theory (DFT) simulations indicate that CoO adsorbs magnesium polysulfides more strongly than Ti<sub>3</sub>C<sub>2</sub> while Ti<sub>3</sub>C<sub>2</sub> is more conductive to Mg<sup>2+</sup> diffusion and transfer than CoO. Coincidentally, use of 1 M electrolyte restrains dissolution of magnesium polysulfides in electrolytes during battery cycling. The experiments indicate that combining Ti<sub>3</sub>C<sub>2</sub>@CoO sulfur hosts and 1 M Mg(TFSI)<sub>2</sub>/AlCl<sub>3</sub>/diglyme electrolyte provides viable MSBs, maintaining discharge capacities of 540 mAh g<sup>-1</sup> after 70 cycles at 100 mA g<sup>-1</sup>. Mechanistic studies indicate that these MSBs work via a S/MgS<sub>x</sub> (x = 2–8) redox process although oxidation of polysulfide to sulfur is not efficient in initial cycling. The systems studied here may offer valuable insights and inspiration in the design of appropriate electrolytes and sulfur-host materials for MSBs.

## 1. Introduction

Higher energy density batteries are now a growing target beyond lithium ion batteries (LIBs) emphasizing efficiency, battery life, weight limitations, and stability but only if they can be cost competitive [1]. Thermodynamics make Mg an obvious candidate to replace Li anodes [2]. In contrast to Li, Mg metal anodes are not plagued by dendrite formation, eliminating such concerns [3]. Additionally, Mg is less air and water sensitive, more abundant in the earth's crust (currently 30x lower cost than Li), and offers a larger theoretical volumetric capacity (3832 mAh cm<sup>-3</sup>) vs Li (2062 mAh cm<sup>-3</sup>) [4]. Also favorable is that Mg has a reduction potential of −2.36 V vs. SHE, higher than Li (−3.0 V vs. SHE) [5].

Extensive efforts are currently focused on improving energy

densities, reversibility and cycling life of magnesium ion batteries (MIBs) since Aurbach first described a rechargeable MIB prototype [6]. Nevertheless, the use of Mg anodes has always been limited by the availability of suitable electrolyte and cathode materials [7,8], with facile passivation of Mg metal surfaces mandated. Furthermore, strong coulombic interactions between Mg<sup>2+</sup> and host matrices lead to sluggish solid-state diffusion [9], rendering cathode materials poor ion conductors. A multitude of materials, including oxides [10,11], chalcogenides [12], and prussian blue [13], have been assessed with conversion materials recently like CuS receiving wide-spread consideration [14]. Motivation centers on their theoretical potential for high capacity, possibly enabling a remarkable upshift in energy density. One such “ideal” conversion material is electrophilic sulfur [15], with a high theoretical volumetric capacity of 3459 mAh cm<sup>-3</sup>, widespread natural

\* Corresponding authors at: National Engineering Research Center of Light Alloy Net Forming, School of Materials Science and Engineering, Shanghai Jiao Tong University, Shanghai, 200240, China (J. Zou).

E-mail addresses: [zoujx@sjtu.edu.cn](mailto:zoujx@sjtu.edu.cn) (J. Zou), [talsdad@umich.edu](mailto:talsdad@umich.edu) (R.M. Laine).

<https://doi.org/10.1016/j.cej.2021.131031>

Received 1 March 2021; Received in revised form 25 May 2021; Accepted 23 June 2021

Available online 29 June 2021

1385-8947/© 2021 Elsevier B.V. All rights reserved.

abundance, and without the kinetic inhibition of  $\text{Mg}^{2+}$  insertion/extraction.

Lewis acid-base complexes are common MIB electrolytes generated by transmetalation reactions between Mg-centered Lewis bases and Al- or B-centered Lewis acids, always exhibiting nucleophilic properties [11]. However, the lack of suitable non-nucleophilic electrolyte compatible with both sulfur and magnesium retards development of magnesium sulfur batteries (MSBs) [16]. To address this issue, non-nucleophilic Hauser bases such as potassium hexamethyldisilazide (KHMDs,  $\text{HMDS} = \text{C}_6\text{H}_{18}\text{NSi}_2$ ) were explored, starting with hexamethyldisilazide magnesium chloride ( $\text{MgHMDSCl}$ ).

The first rechargeable MSB prototype functioned for only two cycles with  $\text{MgHMDSCl}$  and  $\text{AlCl}_3$  in tetrahydrofuran as electrolyte [17], but opened a window for early exploration of MSBs. Later, stable halogen-free  $\text{Mg}(\text{CB}_{11}\text{H}_{11})_2/\text{tetraglyme}$  was prepared as one type of non-nucleophilic electrolytes. Zhao-Karger et al. first used the amide  $\text{Mg}(\text{HMDS})_2/\text{AlCl}_3$  system in combination with different ethereal solvents and an ionic liquid additive [18], finding an improved capacity of 260  $\text{mAh g}^{-1}$  even after 20 cycles. This work was followed by introduction of fluorinated alkoxyborates and alkoxyaluminates Mg salts with reversible discharge capacities of 200  $\text{mAh g}^{-1}$  preserved after 100 cycles [19]. Inorganic electrolytes containing  $\text{MgCl}_2$  and/or  $\text{AlCl}_3$  were also investigated in MSBs [20].

The ionic Mg compound,  $\text{Mg}(\text{TFSI})_2$  [ $\text{TFSI} = \text{bis}(\text{trifluoromethane sulfonyl}) \text{ imide}, \text{C}_2\text{F}_6\text{NO}_4\text{S}_2$ ], dissolved in ethereal solvents was also used as a non-nucleophilic electrolyte for MIBs and MSBs. Ha et al. reported that  $\text{Mg}(\text{TFSI})_2/\text{DME}/\text{diglyme}$  offers potential as a useful MIB electrolyte [21]. Multiple reasons were cited especially the absence of current collector corrosion coincident with a high anodic limit (4.0 V vs.  $\text{Mg}/\text{Mg}^{2+}$ ). Additional advantages include low volatility, easy dissolution in ether solvents permitting ready Mg stripping/plating. However,  $\text{TFSI}^-$  ions were found to be not stable in ether electrolytes where they could react with magnesium metal easily, forming a passive film on the magnesium surface [5]. Wang et al. proved that  $\text{Mg}(\text{TFSI})_2/\text{MgCl}_2/\text{DME}$  was an effective electrolyte for MSBs and high concentrations limited dissolution of magnesium polysulfide in electrolytes during cycling [22]. They also assessed  $\text{Mg}(\text{TFSI})_2/\text{I}_2/\text{DME}$  as an MSB electrolyte [23]. Besides, the ether solvent solubility of  $\text{MgCl}_2$  is relatively lower than  $\text{AlCl}_3$  [24,25].  $\text{AlCl}_3$ , a strong Lewis acid, hinders the formation of a passive film on the magnesium surface [26]. Considering the coordination ability of solvent to  $\text{Mg}^{2+}$ , the viscosity and the ion conductivity, diglyme was selected as the solvents [27]. Thus, the  $\text{Mg}(\text{TFSI})_2/\text{AlCl}_3/\text{diglyme}$  system was chosen for the studies reported here.

MSBs are not expected to behave identically to lithium sulfur batteries (LSBs). However, MSB electrolytes with Li salt additives have also been shown to improve electrochemical performance of MSBs [28–30]. In most cases, the sulfur host materials used in LSBs can serve as relevant models for MSBs [18,31]. For instance, carbon-based materials including carbon black, graphene and carbon nanofibers were successfully used as sulfur host materials for MSBs [17,32,33]. Introduction of carbon-based materials will enhance the conductivity of sulfur containing cathode materials.

Reports on two-dimensional transition metal carbides and carbonitrides, MXenes [34,35], prompted efforts to consider them for MIB applications. Byeon et al. first demonstrated that  $\text{Ti}_3\text{C}_2$  could be used as a cathode material in  $\text{Mg}^{2+}/\text{Li}^+$  hybrid batteries (MLHBs). A capacity of 105  $\text{mAh g}^{-1}$  at 10  $\text{mA g}^{-1}$  was obtained with free-standing and flexible delaminated- $\text{Ti}_3\text{C}_2/\text{CNT}$  paper cathodes [36]. Xu et al. introduced MXene to MIBs by preintercalating a cationic surfactant (hexadecyl trimethyl ammonium bromide, CTAB) into  $\text{Ti}_3\text{C}_2\text{T}_x$  flakes as MIB cathodes [37], showing desirable volumetric capacities of 300  $\text{mAh cm}^{-3}$  at 50  $\text{mA g}^{-1}$ . Recently,  $\text{V}_2\text{C}$  was used as cathodes for MLIBs, displaying reversible capacities of 230  $\text{mAh g}^{-1}$  and cycling life with 82% capacity retention after 480 cycles at 20  $\text{mA g}^{-1}$  [38].

$\text{Ti}_3\text{C}_2$ , as a typical MXene, offers high electronic conductivity (up to 10,000  $\text{S cm}^{-1}$ ) [39], making up for sulfur's low conductivity

( $5.0 \times 10^{-32} \text{ S cm}^{-1}$ ) [40].  $\text{Ti}_3\text{C}_2$  sheets with graphene-like morphology can provide quantities of active sites for sulfur hosting. Moreover, crystalline  $\text{CoO}$  is reported to be conductive and adsorbs intermediate species (lithium polysulfides) in LSBs [41,42], potentially of value in assembling MSBs. Herein, we explore the processing of  $\text{Ti}_3\text{C}_2/\text{CoO}$  heterostructures by *in-situ* formation of  $\text{CoO}$  particles on exfoliated  $\text{Ti}_3\text{C}_2$  surfaces through electrostatic self-assembly and annealing in Argon/Hydrogen(5 %) ( $\text{Ar}/\text{H}_2$ ), followed by introduction of sulfur. These composites were then used with  $\text{Mg}(\text{TFSI})_2/\text{AlCl}_3/\text{diglyme}$  electrolyte to generate MSBs. These results suggest synergistic properties wherein  $\text{Ti}_3\text{C}_2/\text{CoO}$  hosts sulfur in MSBs, contributing to highly reversible, high discharge capacity and good cycling stability compared with other MSBs (see Table S1).

## 2. Experimental sections

### 2.1. Preparation of $\text{Ti}_3\text{C}_2$ and $\text{Ti}_3\text{C}_2\text{-350}$

In a special experiment, 2 g lithium fluoride (99.99 %, Aladdin Reagent) powder was immersed in 30 mL concentrated hydrochloric acid (40 %, Aladdin Reagent). The samples were mixed and stirred at 600 rpm for 5 min. Then, 1 g commercially available  $\text{Ti}_3\text{AlC}_2$  (98 %, Jilin 11 Technology Co., Ltd.) was gradually added to the above samples over the course of 5 min to avoid overheating, followed by continuous stirring at 600 rpm and reacting at 40 °C for 45 h. The reaction products were washed with deionized water and centrifuged for 8–10 times at 4000 rpm until the pH value of the supernatants reached approximately 6. After that, the products dispersed in deionized water were under sonication (90 W) for 4 h when argon bubbled in. Subsequently, the supernatants were decanted followed by freeze-drying to obtain  $\text{Ti}_3\text{C}_2$  flakes. Moreover,  $\text{Ti}_3\text{C}_2\text{-350}$  flakes after annealing in Argon/Hydrogen(5 %) ( $\text{Ar}/\text{H}_2$ ) at 350 °C for 2 h were obtained.

### 2.2. Preparation of $\text{Ti}_3\text{C}_2/\text{CoO}$ composites

40 mL supernatants containing  $\text{Ti}_3\text{C}_2$  (2  $\text{mg mL}^{-1}$ ) were firstly mixed with 40 mL methanol (99.9 %, Aladdin Reagent). Then 0.65 g 2-methylimidazole (98 %, Aladdin Reagent) was added following continuous stirring for 5 min. Simultaneously, 1.16 g  $\text{Co}(\text{NO}_3)_2 \cdot 6\text{H}_2\text{O}$  (99.9 %, Aladdin Reagent) were dissolved rapidly in 40 mL methanol (99.9 %, Aladdin Reagent) by stirring. The obtained solutions were put in above mixtures drop wise resulting in quantities of floccus. The reaction products were washed with deionized water and centrifuged for three times, then to be freeze-dried, which is further demonstrated as  $\text{Ti}_3\text{C}_2/\text{Co-LDH}$  ( $\text{Co-LDH}$ , cobalt-layered double hydroxide) composites. Finally, the samples were annealed under  $\text{Ar}/\text{H}_2$  atmosphere at 350 °C for 2 h to produce end-products as  $\text{Ti}_3\text{C}_2/\text{CoO}$  composites.

### 2.3. Preparation of S- $\text{Ti}_3\text{C}_2/\text{CoO}$ and S-( $\text{Ti}_3\text{C}_2\text{-350}$ ) composites

Typically, prepared  $\text{Ti}_3\text{C}_2/\text{CoO}$  composites or  $\text{Ti}_3\text{C}_2\text{-350}$  (0.4 g) were mixed with 0.6 g sulfur (99.9 %, Aladdin Reagent) by adequate grinding in the mortar. Then, the mixtures were kept at 155 °C under  $\text{Ar}$  atmosphere for 12 h, making sulfur melt into materials interior. Subsequently, S- $\text{Ti}_3\text{C}_2/\text{CoO}$  and S-( $\text{Ti}_3\text{C}_2\text{-350}$ ) composites were obtained separately.

### 2.4. Preparation of electrolytes

Electrolytes were prepared in an  $\text{Ar}$ -filled glove box with the content of water and oxygen less than 0.01 ppm.  $\text{Mg}(\text{TFSI})_2$  (97.0 %, TCI-chemicals) was dried in vacuum at 120 °C for 12 h and diethylene glycol dimethyl ether (diglyme, 99.5 %, Aladdin Reagent) was dried with molecular sieves for 24 h prior to use. Ultra dry  $\text{AlCl}_3$  (99.9 %, Aladdin Reagent) was directly used without further treatment. The electrolyte was prepared by adding  $\text{Mg}(\text{TFSI})_2$  and  $\text{AlCl}_3$  (molar ratio 1:2) in

diglyme and stirring for 12 h. For example, to make 1 M  $\text{Mg}(\text{TFSI})_2/\text{AlCl}_3/\text{diglyme}$  electrolyte, 1 M  $\text{Mg}(\text{TFSI})_2$  and 2 M  $\text{AlCl}_3$  were added to diglyme.

## 2.5. Electrochemical measurements

The coin-type cells (CR2032) were assembled in an argon-filled glove box with the content of water and oxygen less than 0.01 ppm. First, the as-obtained  $\text{S-Ti}_3\text{C}_2/\text{CoO}$  or  $\text{S-(Ti}_3\text{C}_2\text{-350)}$  composites were mixed with PVDF and super P carbon black at mass ratio of 7:1:2. Then NMP was added to the above mixtures to form a slurry, uniformly pasted on the surface of the aluminum foil coated with carbon for vacuum drying at 120 °C for 8 h. The average sulfur loading was 0.5–0.7  $\text{mg cm}^{-2}$  in this study. Polished magnesium foils were made as anodes and the glass fibers (Whatman, GF/A) were posted as the separators.

A LAND CT2001A multichannel battery test system at 25 °C was used for the galvanostatic charge/discharge cycling tests. Electrochemical impedance spectroscopy (EIS) with amplitude of 5 mV and frequency between 100 kHz and 0.1 Hz was implemented on an electrochemical workstation (CHI 660E, Chenhua). Besides, measuring the stability of electrolytes on stainless steel (SS) and Mg stripping/plating were also performed in coin-type cells (CR2032).

## 2.6. Material characterization

X-ray diffraction (XRD) was implemented on a Rigaku Smart Lab diffractometer with  $\text{Cu-K}\alpha$  radiation ( $\lambda = 1.5406 \text{ \AA}$ ) at a scanning rate  $5^\circ \text{ min}^{-1}$ . The morphologies of the products were examined by scanning electron microscopy (SEM, Phenom XL and Mira 3), transmission electron microscopy (TEM, Talos F200X). Energy dispersive X-ray (EDX) spectrometer was attached on SEM. Selected area electron diffraction (SAED) and high resolution transmission electron microscopy (HRTEM) were performed on a Talos F200X microscopy with an accelerating voltage of 200 kV. Thermal gravimetric (TG) analysis was performed on an apparatus (Netzsch STA449F3 Jupiter) under flowing argon atmosphere with a heating rate of  $5^\circ \text{ C min}^{-1}$ . The nitrogen adsorption/desorption isotherm and Barrett-Joyner-Halenda methods were analyzed on a gas sorption analyzer (BELSORP-MAX). Chemical bonding analyses were examined by Fourier transform infrared spectroscopy (FT-IR, Nicolet iS5, Thermo Fisher Scientific Inc. U.S.A.) equipped with a horizontal ATR accessory (Germanium crystal) in an argon-filled glove box. The elemental valence was characterized by X-ray photoelectron spectroscopy equipped with a monochromated  $\text{Al-K}\alpha$  X-ray source (XPS, Ultra DLD, 1486.7 eV). 284.8 eV was used for C 1 s as the reference to calibrate the XPS data. Besides, peak fitting was done using CASA XPS software. The cathodes of cells after 1st discharge/charge were dismantled in the glove box with the content of water and oxygen both less than 0.1 ppm, then to be dried in the vacuum oven at 30 °C for 2 h. The electrodes were directly conducted in XPS measurements. The sulfur contents in all samples were characterized with UV/EV 300 spectrophotometer. The electrodes and electrolytes were diluted with diglyme and transferred to a 2 mm quartz cuvette cell with diglyme as reference. Adsorption at 267 nm was a reference for sulfur.

## 2.7. Computational methods

First-principle calculations were employed to calculate the binding energy by using the plane wave-based VASP code. Projector augmented wave (PAW) [43] pseudopotentials and the Perdew-Burke-Ernzerhof (PBE) version of the generalized gradient approximation (GGA) were applied to describe electron-ion interactions and the electronic exchange correlation effect [44]. Using conjugate-gradient algorithm to conduct ionic relaxation. When the energy change is less than 0.01 eV, the ionic relaxation loop broke. The electronic minimisation algorithm was a fairly robust mixture of the Davidson and RMM-DIIS algorithms. The Kinetic energy cutoff for the planewave basis set was 700 eV. The k-

space was sampled using gamma-centered Monkhorst-Pack scheme with a  $5 \times 5 \times 1$  k-point grid.

The adsorption energy ( $E_{\text{ads}}$ ) between the substrate and the magnesium sulfide is defined as:

$$E_{\text{ads}} = E_{\text{slab+m}} - E_{\text{slab}} - E_{\text{m}}$$

Where  $E_{\text{slab+m}}$ ,  $E_{\text{slab}}$  and  $E_{\text{m}}$  are the ground-state energies of the magnesium sulfide-substrate, substrate ( $\text{CoO}$  or  $\text{Ti}_3\text{C}_2$ ), and magnesium polysulfide, respectively.

## 3. Results and discussion

### 3.1. Preparation of samples

Fig. 1a provides a general overview of the processing steps (see experimental sections) that first generates exfoliated  $\text{Ti}_3\text{C}_2$  and then  $\text{Ti}_3\text{C}_2/\text{CoO}$  composites. Exfoliation was achieved by simply etching  $\text{Ti}_3\text{AlC}_2$  with HCl and LiF to produce multi-layered  $\text{Ti}_3\text{C}_2$  ( $m\text{-Ti}_3\text{C}_2$ ). After sonication following centrifugation, single-layered  $\text{Ti}_3\text{C}_2$  ( $s\text{-Ti}_3\text{C}_2$ ) was dispersed in the supernatant. These single-layered materials could be lyophilized directly to form  $\text{Ti}_3\text{C}_2$  flakes. The  $\text{Ti}_3\text{C}_2$  flakes were then annealed under  $\text{Ar/H}_2$  atmosphere at 350 °C for 2 h to obtain  $\text{Ti}_3\text{C}_2\text{-350}$  flakes.

Alternately, before lyophilizing, the supernatant containing  $s\text{-Ti}_3\text{C}_2$  and deionized water was mixed with methanol and 2-methylimidazole by stirring to produce solution “A”.  $\text{Co}(\text{NO}_3)_2 \cdot 6\text{H}_2\text{O}$  was dissolved rapidly in methanol by stirring to produce solution “B”. When solution B was added to solution A drop wise, flocculated materials were produced and separated from the supernatant, then followed by freeze-drying. The resulting isolated materials were  $\text{Ti}_3\text{C}_2/\text{Co-LDH}$  composites. Finally, the samples were annealed under  $\text{Ar/H}_2$  atmosphere at 350 °C for 2 h, to transform Co-LDH to CoO, resulting in the title materials,  $\text{Ti}_3\text{C}_2/\text{CoO}$  composites.

### 3.2. Characterization of samples

XRD analyses (Fig. 1b) reveal peaks for the (002) and (004) planes of  $\text{Ti}_3\text{C}_2$  flakes but the (104) plane of  $\text{Ti}_3\text{AlC}_2$  at  $39^\circ 2\theta$  disappears, demonstrating successful removal of Al layers forming  $\text{Ti}_3\text{C}_2$  [45]. The XRD of  $\text{Ti}_3\text{C}_2\text{-350}$  shows that the intensities of the (002) and (004) planes increase slightly and peaks narrow apparently compared with those of  $\text{Ti}_3\text{C}_2$ , suggesting that crystallinity improves after  $\text{Ar/H}_2$  annealing. This can be ascribed to the removal of  $\text{Ti}_3\text{C}_2$  surface functional groups ( $-\text{O}$ ,  $-\text{OH}$  and  $-\text{F}$ ) during annealing [46]. Also, the (002) plane of  $\text{Ti}_3\text{C}_2\text{-350}$  shifts to  $8.6^\circ 2\theta$ , higher than that of  $\text{Ti}_3\text{C}_2$  ( $6.8^\circ 2\theta$ ), demonstrating a decrease in layer-spacing.

The interaction of  $\text{Co}^{2+}$  with the electronegative  $\text{Ti}_3\text{C}_2$  flakes [40] drives electrostatic self-assembly (Fig. S1) forming  $\text{Ti}_3\text{C}_2/\text{Co-LDH}$  composites as seen by XRD (Fig. S2) [47], where the interplanar spacings match well with those of (003), (006), (100), (102), (110) and (113) planes for Co-LDH (JCPDs. card 46–0605) and that of (002) plane for  $\text{Ti}_3\text{C}_2$  [31]. After annealing in  $\text{Ar/H}_2$ , Co-LDH transforms into CoO *in-situ* giving the target  $\text{Ti}_3\text{C}_2/\text{CoO}$  composites, whose diffraction peaks match well with what might be considered composites of  $\text{Ti}_3\text{C}_2$  and CoO (JCPDs. card 75–0418) presented in Fig. 1c, thereby indicating that the preparation process has no effect on the  $\text{Ti}_3\text{C}_2$  phase. However, some  $\text{Ti}_3\text{C}_2$  diffraction peaks, e.g. the (004) plane, are not found in the pattern. In some cases,  $\text{Ti}_3\text{C}_2$  peaks with low intensities are covered by CoO peaks with higher intensities (higher  $z$  value). Also, the absence of typical peaks for  $\text{Ti}_3\text{C}_2$  layer structures may arise as CoO nanoparticles form on  $\text{Ti}_3\text{C}_2$  flakes, especially for the (002) plane along the  $c$ -axis. After introduction of sulfur, characteristic sulfur peaks for  $\text{S-Ti}_3\text{C}_2/\text{CoO}$  and  $\text{S-(Ti}_3\text{C}_2\text{-350)}$  composites are seen in Fig. 1c and Fig. S3, indicating successful impregnation of sulfur into  $\text{Ti}_3\text{C}_2/\text{CoO}$  and  $\text{Ti}_3\text{C}_2\text{-350}$  hosts, respectively.



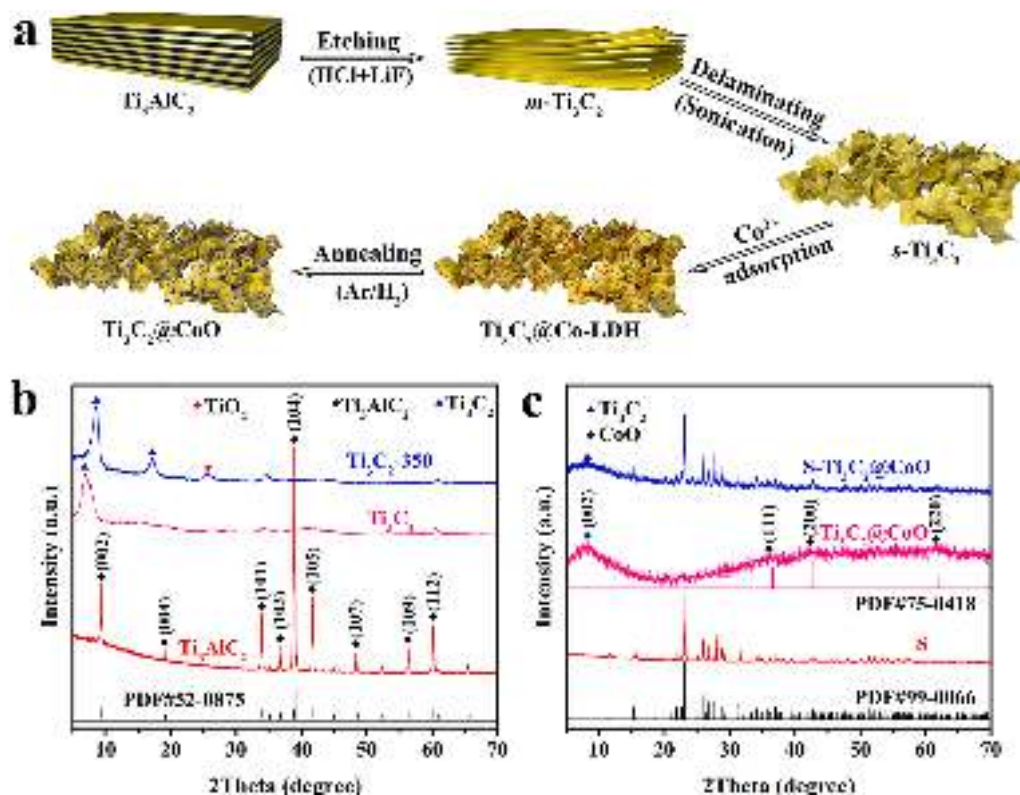


**Fig. 1.** (a) General morphologies and methods used to prepare  $\text{Ti}_3\text{C}_2$  and  $\text{Ti}_3\text{C}_2@\text{CoO}$ . (b) XRD patterns of  $\text{Ti}_3\text{AlC}_2$ ,  $\text{Ti}_3\text{C}_2$ , and  $\text{Ti}_3\text{C}_2\text{-350}$ . (c) XRD patterns of sulfur,  $\text{Ti}_3\text{C}_2@\text{CoO}$ , and  $\text{S-Ti}_3\text{C}_2@\text{CoO}$ .

TG under Ar atmosphere was used to quantify the sulfur content in  $\text{S-Ti}_3\text{C}_2@\text{CoO}$  and  $\text{S-Ti}_3\text{C}_2\text{-350}$  composites. As shown in Fig. S4, mass loss occurs mainly in the 150–350 °C range, as S sublimes indicating sulfur contents of 59.2, 58.4 and 100.0 % in  $\text{S-Ti}_3\text{C}_2@\text{CoO}$ ,  $\text{S-Ti}_3\text{C}_2\text{-350}$  and S, respectively.

Sample morphologies were investigated by SEM and TEM. Fig. 2a and b indicate that  $\text{Ti}_3\text{C}_2@\text{Co-LDH}$  and  $\text{Ti}_3\text{C}_2@\text{CoO}$  composites show similar layered morphologies and flake sizes. Fig. S5 demonstrates a distribution of C, Ti, Co, O for  $\text{Ti}_3\text{C}_2@\text{Co-LDH}$  while no N is detected owing to its quite low content. After annealing in  $\text{Ar/H}_2$ , Co-LDH transforms *in-situ* to CoO, resulting in the formation of  $\text{Ti}_3\text{C}_2@\text{CoO}$ , also showing a homogenous element distribution of C, Ti, Co, O (Fig. S6). However, the flake sizes of  $\text{Ti}_3\text{C}_2$  (Fig. S7) and  $\text{Ti}_3\text{C}_2\text{-350}$  (Fig. S8) increase apparently. The diffusion time  $t$  ( $t = L^2/D$ ) for  $\text{Mg}^{2+}$  diffusion in a solid electrode is proportional to the square of the diffusion length,  $L$ , and inversely proportional to the diffusion coefficient,  $D$ . Smaller flakes with shorter diffusion lengths should improve the diffusion kinetics of  $\text{Mg}^{2+}$  within a particular flake [48]. The specific surface areas (SSAs) and porosities of  $\text{Ti}_3\text{C}_2@\text{CoO}$  and  $\text{Ti}_3\text{C}_2\text{-350}$  samples were characterized by  $\text{N}_2$  adsorption/desorption as these properties play an important role in the battery performance of electroactive materials. As seen in Fig. S9 and Table S2, the Brunauer-Emmett-Teller (BET) SSAs of  $\text{Ti}_3\text{C}_2@\text{CoO}$  and  $\text{Ti}_3\text{C}_2\text{-350}$  are 84 and 57  $\text{m}^2 \text{g}^{-1}$  respectively. Using the Barrett-Joyner-Halenda (BJH) method, one peak in the pore size distribution for  $\text{Ti}_3\text{C}_2@\text{CoO}$  is seen for pore diameter of 3.8 nm while that for  $\text{Ti}_3\text{C}_2\text{-350}$  is 4.3 nm. These results indicate that  $\text{Ti}_3\text{C}_2@\text{CoO}$  with larger SSAs and smaller average pore sizes could be a better choice for infiltration of sulfur in the host materials compared with  $\text{Ti}_3\text{C}_2\text{-350}$ . In addition, Fig. 2c suggests that  $\text{Ti}_3\text{C}_2@\text{CoO}$  flakes resemble graphene. It indicates that the introduction of CoO to form  $\text{Ti}_3\text{C}_2@\text{CoO}$  flakes suppresses  $\text{Ti}_3\text{C}_2$  agglomeration during freeze-drying.

Fig. S10 shows typical TEM, HRTEM and SAED images of  $\text{Ti}_3\text{C}_2@\text{Co-LDH}$  composites. Co-LDH seems to cover the  $\text{Ti}_3\text{C}_2$  surface. The

dominant lattice fringes in HRTEM image have interplanar spacings of 0.373 and 0.256 nm, corresponding to the (006) and (102) planes of Co-LDH, respectively. The SAED diffraction rings can be indexed as (110) and (102) planes of Co-LDH. These results further confirm the presence of the Co-LDH phase, agreeing well with XRD, SEM and EDX results. Moreover, TEM images (Fig. 2e and f) provide examples of CoO nanoparticles ( $\approx 5$  nm apparent particle size) forming on exfoliated  $\text{Ti}_3\text{C}_2$  layers, as further confirmed by HRTEM (Fig. 2g), SAED (Fig. 2h) and HAADF (Fig. S11). The dominant lattice fringes in HRTEM have spacings of 0.214 and 0.248 nm, corresponding to the (200) and (111) planes of CoO. Besides, d-spacings of  $\text{Ti}_3\text{C}_2$  are measured to be 1.059 nm for the (002) plane and 0.468 nm for (004) plane. The SAED diffraction rings are indexed as (200), (220), (111) planes of CoO, respectively.

After sulfur impregnation, the  $\text{S-Ti}_3\text{C}_2@\text{CoO}$  composites are discerned easily with rough surface (Fig. 2d and i), similar to  $\text{S-Ti}_3\text{C}_2\text{-350}$  composites seen in Figs. S12a and b. Moreover, Fig. 2j–o and Table S3 disclose a homogeneous distribution of C, O, Ti, Co, S. Mapping results for  $\text{S-Ti}_3\text{C}_2\text{-350}$  composites in Figs. S12c–h and Table S4 reveal homogeneous distribution of C, O, F, Ti and S. These results verify the successful immobilization of sulfur in  $\text{Ti}_3\text{C}_2@\text{CoO}$  and  $\text{Ti}_3\text{C}_2\text{-350}$  hosts.

### 3.3. Electrochemical performance of MSBs

The influence of diglyme-based solvent on coordination with  $\text{Mg}^{2+}$  was characterized by FT-IR. If an interaction occurs in the samples, a peak corresponding to a specific functional group in the FT-IR spectrum shifts toward either higher or lower wavenumber, sometimes a new peak appears [49].  $\text{Mg}^{2+}$  solvation via ion–dipole interactions can be realized by the use of diglyme with a high donor number of 19.5  $\text{kcal mol}^{-1}$  [21]. Fig. S13 shows a clear disparity among all samples. The peaks at 1055 and 1210  $\text{cm}^{-1}$  are typical regions of the S–O and C–F stretching of  $\text{Mg}(\text{TFSD})_2$ . As for diglyme solvent, the peak at 852  $\text{cm}^{-1}$  is ascribed to characteristic band of  $\text{CH}_2$  rocking vibration coupled with C–O

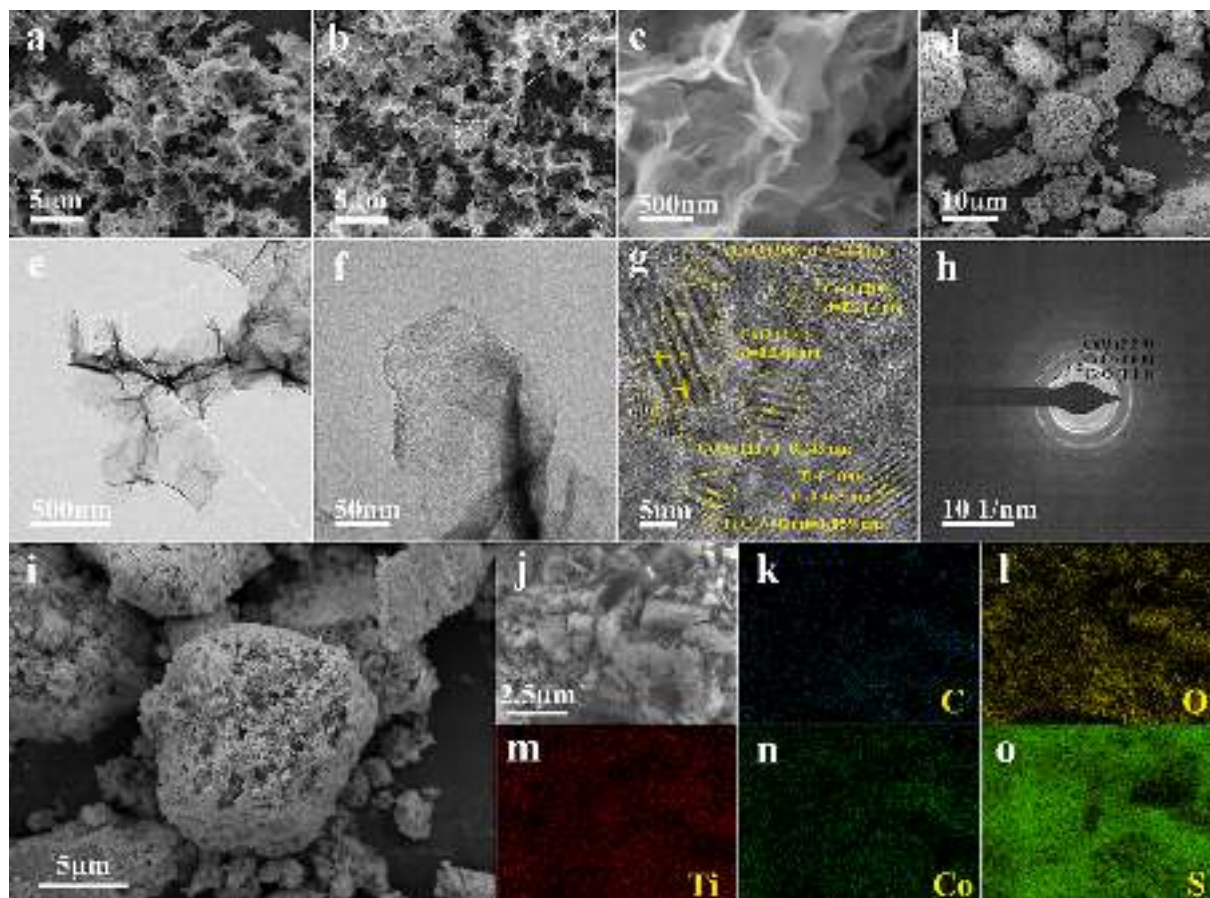


**Fig. 2.** SEM images of (a)  $\text{Ti}_3\text{C}_2@\text{Co-LDH}$  composites, (b, c)  $\text{Ti}_3\text{C}_2@\text{CoO}$  composites from different scales and (d)  $\text{S-Ti}_3\text{C}_2@\text{CoO}$  composites. (e, f) TEM, (g) HRTEM images and (h) SAED pattern of  $\text{Ti}_3\text{C}_2@\text{CoO}$  composites. (i, j) SEM images from different scales and (k-o) EDX results of  $\text{S-Ti}_3\text{C}_2@\text{CoO}$  composites.

stretching accompanied by the peak at  $1104\text{ cm}^{-1}$  in the C-O-C region. When  $\text{Mg}(\text{TFSI})_2$  added to the diglyme, a new weak peak at  $1080\text{ cm}^{-1}$  in the C-O-C region is produced. However, this peak shows little weaker when  $\text{AlCl}_3$  added further while the intensity will increase with the increasing concentration of  $\text{Mg}(\text{TFSI})_2/\text{AlCl}_3$  in diglyme. This result persuasively indicate that diglyme could solvate  $\text{Mg}^{2+}$  sufficiently, which is little affected by  $\text{AlCl}_3$  but greatly influenced by the concentration of the salts. Moreover, the pronounced new peak at  $1041\text{ cm}^{-1}$  is assigned to C-C stretching vibration coupled with the C-O stretching of diglyme when  $\text{Mg}(\text{TFSI})_2$  added to the diglyme solvent. For a comparison, the interaction between  $\text{Mg}^{2+}$  and diglyme exhibits no obvious affection on the peak at  $852\text{ cm}^{-1}$ . Nevertheless, C-O groups will coordinate with  $\text{Mg}^{2+}$  when  $\text{Mg}(\text{TFSI})_2$  mixed with diglyme, thus producing a new peak at  $874\text{ cm}^{-1}$ , whose intensity increases with the creasing salt concentration. Specifically, these results illuminate that solvation between  $\text{Mg}^{2+}$  and diglyme should be realized while it can be greatly influenced by the salt concentration but little influenced by the addition of  $\text{AlCl}_3$ . Our FT-IR results suggest that diglyme can solvate  $\text{Mg}^{2+}$  from  $\text{Mg}(\text{TFSI})_2$  sufficiently, and little affected by the addition of  $\text{AlCl}_3$  but greatly influenced by the concentration of the  $\text{Mg}(\text{TFSI})_2/\text{AlCl}_3$  salts in diglyme.

The cyclic voltammetry (CV) data in Fig. S14a illustrate clearly that as-synthesized electrolytes with different molar concentrations enable reversible Mg stripping/plating. The oxidative stability of the electrolytes was also investigated by linear sweep voltammetry (LSV) in Fig. S14b. With the SS electrode, 1 M electrolyte is stable up to 2.8 V, showing a better oxidation tolerance than 0.25 M electrolyte (2.4 V). Proof of dendrite-free surfaces is also a requisite for MSBs. The Pt foil as working electrode was held at  $-1.2\text{ V}$  using 1 M electrolyte for 1 h with Mg foil as reference and counter electrodes. The SEM image (Fig. S15a)

shows the deposits those are smooth and dendrite-free consisting of substantial spherical structures in good agreement with previous reports [21]. EDX results (Fig. S15c) reveal strong Mg and O peaks for the Mg deposits on Pt foil. The deposits on the Pt foil were further investigated by using XPS. Through Mg 2p spectra (Fig. S16), it is found that the deposits' surfaces have plenty species of  $\text{MgO}$ ,  $\text{Mg}(\text{OH})_2$  and Mg, which is probably ascribed to the passivation layer forming on the deposited Mg [50,51]. The Mg foil presented in Fig. S15b shows a smooth surface with a few pits with some protruding Mg deposits. EDX results in Fig. S15d show no obvious morphological variations at the Mg foil surface, suggesting that Mg can deposit effectively on Pt foil in the 1 M electrolyte without dendrite formation.

The electrochemical performances of  $\text{S-Ti}_3\text{C}_2@\text{CoO}$  and  $\text{S-Ti}_3\text{C}_2\text{-350}$  cathodes were investigated in CR2032 coin cells with Mg foils as anodes with a ternary electrolyte consisting of  $\text{Mg}(\text{TFSI})_2$  and  $\text{AlCl}_3$  in diglyme. Fig. 3a and Fig. S17 display galvanostatic discharge/charge curves under a protocol with a cut-off of  $800\text{ mAh g}^{-1}$  and a discharge voltage to  $0.5\text{ V}$  at  $100\text{ mA g}^{-1}$  during 1st, 2nd, 3rd, 10th, 20th, 30th and 40th cycles for cells using 1 M electrolyte and  $\text{S-Ti}_3\text{C}_2@\text{CoO}$  cathodes. During the first discharge, the cathode delivers a total capacity as high as  $1500\text{ mAh g}^{-1}$ . Thereafter, the first charge process shows voltage climbing to  $1.9\text{ V}$  with a capacity of  $\approx 295\text{ mAh g}^{-1}$ , followed by a curve up to  $800\text{ mAh g}^{-1}$ . This unusual upper plateau is likely caused by a shuttle effect from soluble sulfides similar to what is observed in early LSB research [52]. For the second cycle, the electrochemical curve changes with a desirable extension. The discharge capacity decreases to  $1070\text{ mAh g}^{-1}$ . Solid electrolyte interfaces including magnesium oxide form during cycling at the price of consuming some electrolytes [32,53,54], thus causing capacity decaying. The discharge capacity in the 3th cycle is  $970\text{ mAh g}^{-1}$ . During 10th, 20th, 30th and 40th cycles,



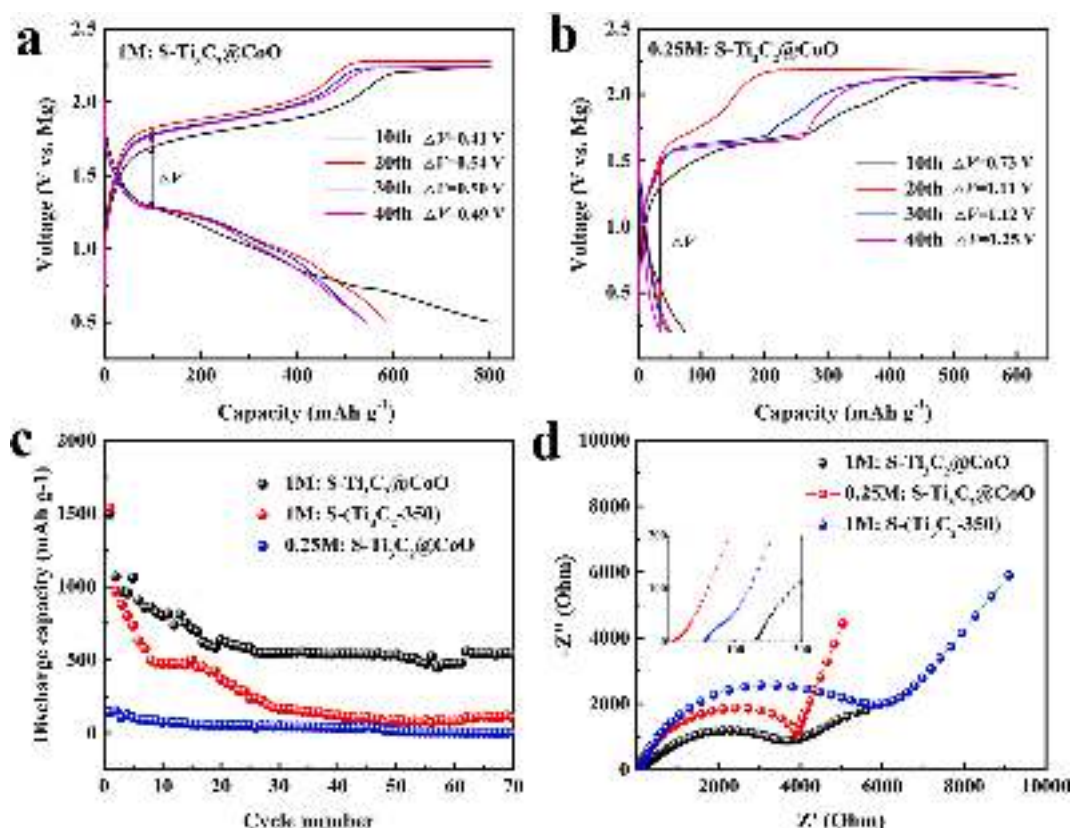


**Fig. 3.** Electrochemical evaluation for MSBs. (a) Discharge and charge profiles of cells using S-Ti<sub>3</sub>C<sub>2</sub>@CoO electrodes and 1 M electrolyte during 10th, 20th, 30th and 40th cycles at 100 mA g<sup>-1</sup>. (b) Discharge and charge profiles of cells using S-Ti<sub>3</sub>C<sub>2</sub>@CoO electrodes and 0.25 M electrolyte during 10th, 20th, 30th and 40th cycles at 100 mA g<sup>-1</sup>. (c) Cycling performance comparison for cells at 100 mA g<sup>-1</sup>. (d) Electrochemical impedance spectra (EIS) of the cells and inset is the enlarged image of low impedance.

the discharge capacities are 801, 635, 543 and 540 mAh g<sup>-1</sup>, respectively.

Nevertheless, the cells exhibit poor electrochemical performance using 0.25 M electrolyte (Fig. 3b and Fig. S18). At 100 mA g<sup>-1</sup>, the voltage decreases to 0.2 V with a capacity of 140 mAh g<sup>-1</sup> for the first discharge and increases to 1.4 V for the first charge, then climbs to 1.88 V with a cut-off capacity of 600 mAh g<sup>-1</sup>. The discharge capacities for the 2nd and 3rd cycles are 150 and 100 mAh g<sup>-1</sup>. The discharge/charge curves during 10th, 20th, 30th and 40th cycles suggest that 0.25 M electrolyte triggers serious shuttling of magnesium polysulfides.

Moreover, the S-Ti<sub>3</sub>C<sub>2</sub>@CoO cathode cell using 1 M electrolyte exhibits a voltage hysteresis (ΔV) decrease to 0.49 V after 40 cycles, much lower than that using 0.25 M electrolyte (1.25 V). Simultaneously, ΔV of the cell does not decrease obviously and shows a low discharge capacity. The ΔV of cell using S-(Ti<sub>3</sub>C<sub>2</sub>-350) cathode and 1 M electrolyte is 0.31 V during first cycle but increases to 1.22 V after 40 cycles, indicating serious polarization (Fig. S19), Fig. S20. These results further indicate the good compatibility between 1 M electrolyte and S-Ti<sub>3</sub>C<sub>2</sub>@CoO electrodes. Also, MSBs with higher electrolyte concentrations show much better electrochemical performance than those with low concentrations, likely because of less dissolution of magnesium polysulfide [22].

Cells using 1 M electrolyte and S-(Ti<sub>3</sub>C<sub>2</sub>-350) cathodes display discharge capacities of 1540, 970 and 880 mAh g<sup>-1</sup> for 1st, 2nd and 3rd cycles at 100 mA g<sup>-1</sup>. However, the capacity decreases to 120 mAh g<sup>-1</sup> after 40 cycles. Fig. 3c shows discharge capacities of 540, 106 and 3 mAh g<sup>-1</sup> for the three types of cells after 70 cycles, respectively. In addition, Fig. S21 shows the cycling performance of the magnesium ion batteries (MIBs) using Ti<sub>3</sub>C<sub>2</sub>@CoO cathode and 1 M electrolyte at 100 mA g<sup>-1</sup> for 100 cycles. The MIB display a reversible capacity of 11 mAh g<sup>-1</sup>, thus

contributing a little to the capacity of our MSBs. Moreover, Figs. S22a and b show that cells using 1 M electrolyte and S-Ti<sub>3</sub>C<sub>2</sub>@CoO cathodes display discharge capacities of 1285, 928 and 764 mAh g<sup>-1</sup> for 1st, 2nd and 3rd cycles at 200 mA g<sup>-1</sup>, respectively. The capacity decreases to 465 mAh g<sup>-1</sup> after 40 cycles. When current density increases to 1000 mA g<sup>-1</sup>, the cells show a discharge capacity of 154 mAh g<sup>-1</sup> after 40 cycles and even maintain 102 mAh g<sup>-1</sup> after 1000 cycles, as shown in Figs. S22c and d. The above results indicate that Ti<sub>3</sub>C<sub>2</sub>@CoO composites greatly improve the utility of MXene materials as sulfur host materials in MSBs.

To determine the conductivity and ion transport properties, Fig. 3d compares the Nyquist plots. Each plot consists of two parts, a semicircle at high frequency and a straight line at low frequency, which correspond to charge transfer resistance ( $R_{ct}$ ) and Warburg impedance ( $W$ ) associated with Mg<sup>2+</sup> diffusion in the electrolyte and bulk electrode [35,55].  $R_{ct}$  is a combination of an electrolyte-accessible area and electrical conductivity of the electrode. A larger electroactive surface area leads to a lower  $R_{ct}$ . From Fig. 3d, cells using S-Ti<sub>3</sub>C<sub>2</sub>@CoO cathodes and 1 M electrolyte offer an  $R_{ct}$  value of 4770 Ω, which is lower than those using S-(Ti<sub>3</sub>C<sub>2</sub>-350) cathodes and 1 M electrolyte (6621 Ω) and those using S-Ti<sub>3</sub>C<sub>2</sub>@CoO cathodes and 0.25 M electrolyte (4853 Ω), thereby exhibiting a lower charge transfer resistance. Meanwhile, the electronic resistance ( $R_s$ ) of the cells using S-Ti<sub>3</sub>C<sub>2</sub>@CoO cathodes and 0.25 M electrolyte (26 Ω) is lower than those using S-Ti<sub>3</sub>C<sub>2</sub>@CoO cathodes and 1 M electrolyte (114 Ω) and those using S-(Ti<sub>3</sub>C<sub>2</sub>-350) cathodes and 1 M electrolyte (97 Ω). These results indicate that 1 M electrolyte and introduction of CoO favors migration of Mg<sup>2+</sup> and electron transfer at electrolyte/electrode interfaces.

### 3.4. Mechanistic studies of MSBs

Magnesium polysulfide adsorption visual experiments were performed with the red magnesium polysulfide solution prepared according to the previous literature [56]. As evidence, the properties of the  $\text{Ti}_3\text{C}_2\text{-350}$  and  $\text{Ti}_3\text{C}_2\text{@CoO}$  to trap magnesium polysulfide are shown in Fig. S23. In detail, polysulfide solution mixed with  $\text{Ti}_3\text{C}_2\text{@CoO}$  becomes colorless after 30 min, while polysulfide solution mixed with  $\text{Ti}_3\text{C}_2\text{-350}$  becomes a little colorless after 12 h. The optical magnesium polysulfide adsorption effect is different, indicating that  $\text{Ti}_3\text{C}_2\text{@CoO}$  could adsorb magnesium polysulfide more strongly than  $\text{Ti}_3\text{C}_2$ .

To further probe the redox reactions that occur during discharge/charge processes in MSBs, pristine  $\text{S-Ti}_3\text{C}_2\text{@CoO}$  cathode and cathodes after discharge/charge from dismantled cells with 1 M electrolyte running at  $100 \text{ mA g}^{-1}$  were conducted by XPS. Fig. 4 displays S 2p spectra of the cathodes in different states. With a binding energy separation of 1.16 eV for 2p<sub>1/2</sub> and 2p<sub>3/2</sub>, the same full width at half maximum (FWHM) and an area ration of 2:1, the S 2p spectra were fitted to spin-orbit-split doublets respectively. The peaks at higher binding energy for 2p<sub>3/2</sub> (169 eV and 167 eV) in the pristine cathode can be ascribed to the formation of  $\text{S}^{6+}\text{-O}$  and  $\text{S}^{4+}\text{-O}$ , originating from the oxidation of surface sulfur during sample preparation and S-O bond in  $\text{Mg(TFSI)}_2$ . The pristine cathode gives rise to a peak at 163.7 eV, typical for S 2p<sub>3/2</sub> of S and lower than that previously reported [29], indicating the confinement of small S molecules by  $\text{Ti}_3\text{C}_2\text{@CoO}$  hosts. When discharged to 0.5 V, the peak for S 2p<sub>3/2</sub> of S reduces greatly in intensity, indicating the consumption of sulfur during discharge. The peaks at 167 eV and 169 eV also result from the electrolyte-related products (TFSI/ $\text{MgSO}_4$ ) and their reduction species (TFSI/ $\text{MgSO}_3$ ). Additionally, a new

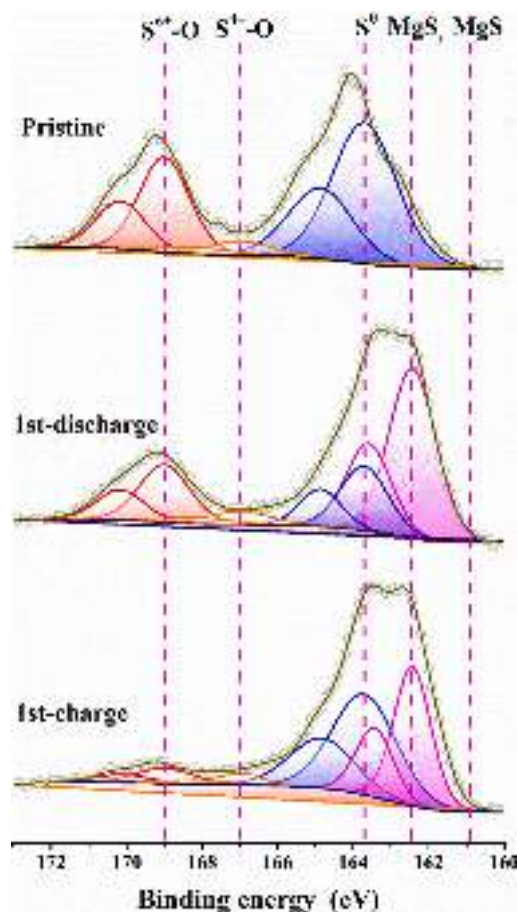


Fig. 4. High-resolution XPS analysis. S 2p of the  $\text{S-Ti}_3\text{C}_2\text{@CoO}$  cathodes: pristine, 1st discharge to 0.5 V and 1st charge to  $800 \text{ mAh g}^{-1}$ .

peak at 162.5 eV between those for S (163.7 eV) and for  $\text{MgS}$  (161.9 eV) is observed owing to S 2p<sub>3/2</sub> for  $\text{MgS}_x$  ( $x = 2-8$ ) formation during discharge [15]. The formation of magnesium polysulfide was also confirmed by UV/Vis analysis of the discharged  $\text{S-Ti}_3\text{C}_2\text{@CoO}$  cathodes (Fig. S24), where the absorbance appears in the range of 350–400 nm with a new peak emerging at 363 nm, supporting the formation of magnesium polysulfide after discharge [22]. After recharge to a cut-off capacity of  $800 \text{ mAh g}^{-1}$ , the 163.7 eV component of S 2p<sub>3/2</sub> for S is recovered at the expense of  $\text{MgS}_x$  ( $x = 2-8$ ). However, the peak at 162.5 eV doesn't disappear completely, implying that  $\text{MgS}_x$  ( $x = 2-8$ ) is just partly converted to elemental S.

UV/Vis results further verify the existence of magnesium polysulfide in  $\text{S-Ti}_3\text{C}_2\text{@CoO}$  cathodes after the 1st charge. Meanwhile, the peaks at 167 and 169 eV decrease in intensity after charging. The XPS signal for Mg 2p emerges after the 1st discharge, indicating reaction between Mg and  $\text{S-Ti}_3\text{C}_2\text{@CoO}$  cathodes (Fig. S25a). The interaction or catalytic effect of Co on magnesium polysulfide may cause the shift of Co 2p peaks toward lower binding energies after 1st cycle (Fig. S25b) [16]. The XPS results indicate that the main 1st discharge product is  $\text{MgS}_x$  ( $x = 2-8$ ), while it is not converted completely to element sulfur after the 1st charge. These results are consistent with discharge/charge curves during the 1st cycle.

The  $\text{MgS}$  chemisorption capability difference between  $\text{CoO}$  and  $\text{Ti}_3\text{C}_2$  was also modeled using density functional theory (DFT) simulations. The (200) plane of  $\text{CoO}$  and (002) plane of  $\text{Ti}_3\text{C}_2$  were chosen as the representative crystalline planes for these simulations, because the exposed atoms of (200) planes for  $\text{CoO}$  have a Co/O ratio of 1:1 and atoms of (002) planes for  $\text{Ti}_3\text{C}_2$  are external with two dimensional micro-structure. Fig. 5a and b show that the calculated adsorption energy ( $E_{\text{ads}}$ ) between  $\text{CoO}$  and  $\text{MgS}_8$  is  $-1.78 \text{ eV}$ , lower than that between  $\text{Ti}_3\text{C}_2$  and  $\text{MgS}_8$  ( $-0.30 \text{ eV}$ ). As for  $\text{MgS}_4$ ,  $\text{CoO}$  and  $\text{Ti}_3\text{C}_2$  show  $E_{\text{ads}}$  of  $-2.54$  and  $-1.24 \text{ eV}$ , respectively (Fig. 5c and d). Fig. 5e, f show the calculated  $E_{\text{ads}}$  between  $\text{CoO}$  and  $\text{MgS}$  is  $-2.07 \text{ eV}$ , lower than that between  $\text{Ti}_3\text{C}_2$  and  $\text{MgS}$  ( $-0.83 \text{ eV}$ ). These results are also presented in Fig. S26 and Fig. 5g. However, MXenes always have  $\text{T}_x$  surface functional groups including O, OH and F [57,58]. Fig. S27 and Table S5 show that the calculated  $E_{\text{ads}}$  between  $\text{Ti}_3\text{C}_2\text{T}_x$  ( $\text{T} = \text{F}, \text{OH}$  and  $\text{O}$ ) and  $\text{MgS}_x$  ( $x = 8, 4, 1$ ) are higher than those between  $\text{Ti}_3\text{C}_2$  and  $\text{MgS}_x$  ( $x = 8, 4, 1$ ). This is probably owing to the repulsive force between F, O and S atoms, confirming that  $\text{T}_x$  groups can affect the DFT results [59]. Thus, the stronger adsorption of magnesium polysulfide by  $\text{CoO}$  than  $\text{Ti}_3\text{C}_2$  and  $\text{Ti}_3\text{C}_2\text{T}_x$  ( $\text{T} = \text{F}, \text{OH}$  and  $\text{O}$ ), leads to more effective suppression of the shuttle effect for  $\text{Ti}_3\text{C}_2\text{@CoO}$  than that for  $\text{Ti}_3\text{C}_2$  alone, hence favoring the better cycling behavior in MSBs.

In addition, Mg ion diffusion pathways on  $\text{CoO}$  and  $\text{Ti}_3\text{C}_2$  are also showcased in Fig. S28. The diffusion energy barriers were calculated to be 0.39 and 0.05 eV for  $\text{CoO}$  and  $\text{Ti}_3\text{C}_2$ , respectively. It indicate that  $\text{Ti}_3\text{C}_2$  improve smooth Mg ion diffusion and transfer for fast reaction kinetics. However,  $\text{CoO}$  can adsorb magnesium polysulfides more strongly than sole  $\text{Ti}_3\text{C}_2$ . Likewise, high concentration  $\text{Mg(TFSI)}_2$ -based electrolyte also prevents magnesium polysulfide dissolution [22], as witnessed by the better properties found for cells using 1 M electrolyte and  $\text{S-Ti}_3\text{C}_2\text{@CoO}$  cathodes. These synergetic effects ensured the highly reversible electrochemical reaction and high sulfur utilization for MSBs working via a  $\text{S/MgS}_x$  ( $x = 2-8$ ) redox process, which is favorably illustrated in Fig. 5h.

## 4. Conclusions

Etching  $\text{Ti}_3\text{AlC}_2$  via HCl and LiF treatment produces supernatant containing single-layer  $\text{Ti}_3\text{C}_2$  flakes. After freeze-drying, the  $\text{Ti}_3\text{C}_2$  flakes agglomerate seriously. Through annealing in  $\text{Ar/H}_2$ ,  $\text{Ti}_3\text{C}_2\text{-350}$  flakes are produced. When negatively charged  $\text{Ti}_3\text{C}_2$  from the supernatant self-assembled electrostatically with  $\text{Co}^{2+}$ ,  $\text{Ti}_3\text{C}_2\text{@Co-LDH}$  composite flakes form. After annealing in  $\text{Ar/H}_2$ ,  $\text{Ti}_3\text{C}_2\text{@CoO}$  composite flakes are obtained with a much smaller size than  $\text{Ti}_3\text{C}_2$  and  $\text{Ti}_3\text{C}_2\text{-350}$  flakes,



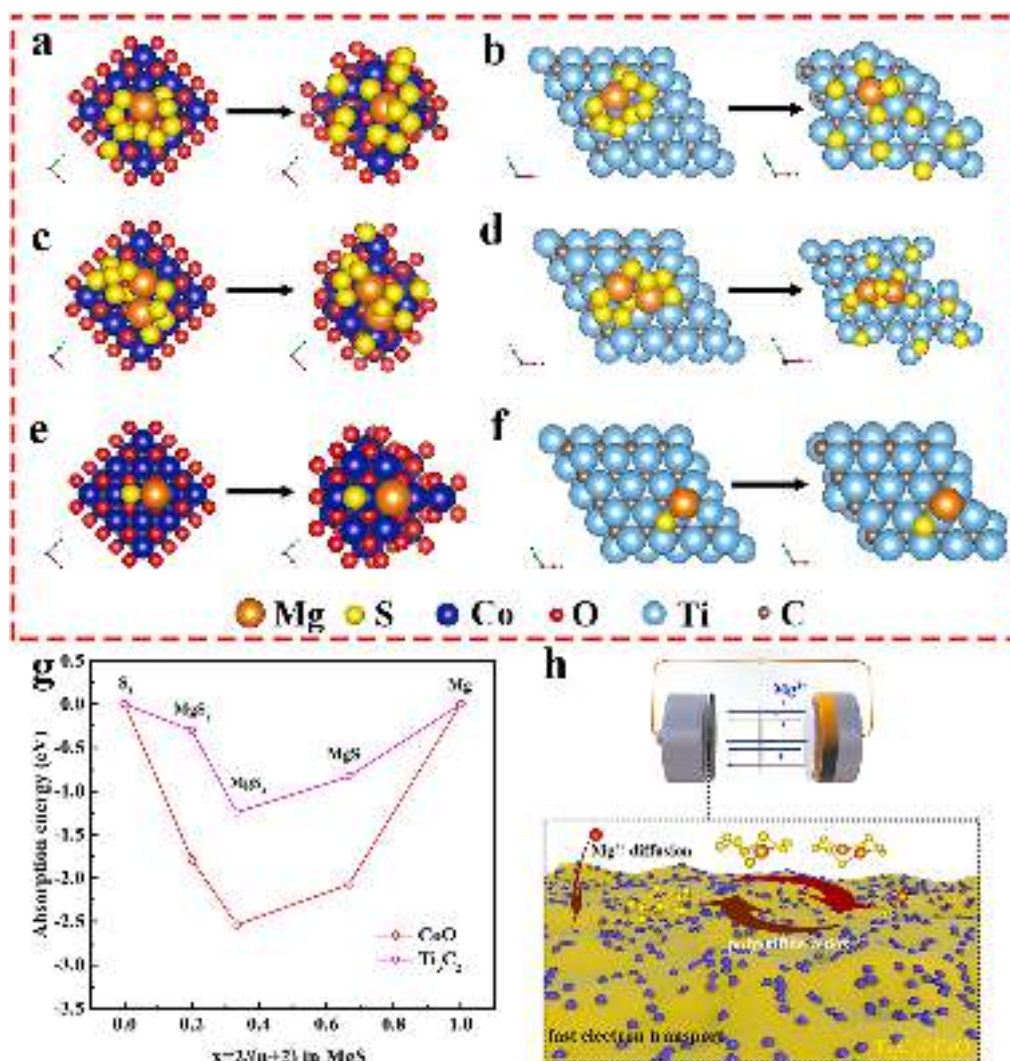


**Fig. 5.** Density functional theory (DFT) calculation (top view) of the adsorption models for (a) MgS<sub>8</sub>, (c) MgS<sub>4</sub> and (e) MgS on the CoO (200) facet. DFT calculation of the adsorption models for (b) MgS<sub>8</sub>, (d) MgS<sub>4</sub> and (f) MgS on the Ti<sub>3</sub>C<sub>2</sub> (002) facet (Vienna Ab-Initio Simulation Package (VASP)). (g) Calculated  $E_{\text{ads}}$  results. (h) Magnesium polysulfide redox mechanism of the S-Ti<sub>3</sub>C<sub>2</sub>@CoO electrode.

promoting the motivation of  $\text{Mg}^{2+}$ . Owing to small size and petal-like morphology, Ti<sub>3</sub>C<sub>2</sub>@CoO flakes should provide more sites for sulfur hosting than Ti<sub>3</sub>C<sub>2</sub> flakes. Besides, Ti<sub>3</sub>C<sub>2</sub>@CoO flakes form a conductive framework for sulfur. DFT calculations verify that CoO has stronger adsorption towards magnesium polysulfides evidenced during battery cycling than Ti<sub>3</sub>C<sub>2</sub>, thus alleviating shuttle effects. Moreover, Ti<sub>3</sub>C<sub>2</sub> is more beneficial to  $\text{Mg}^{2+}$  diffusion and transfer than CoO.

Cells using S-Ti<sub>3</sub>C<sub>2</sub>@CoO cathodes and 1 M Mg(TFSI)<sub>2</sub>/AlCl<sub>3</sub>/diglyme electrolyte display a first discharge capacity as high as 1500 mAh g<sup>-1</sup> and maintain 540 mAh g<sup>-1</sup> after 70 cycles at 100 mA g<sup>-1</sup>, which is higher than those using S-(Ti<sub>3</sub>C<sub>2</sub>-350) cathodes and 1 M electrolyte (106 mAh g<sup>-1</sup>) and those using S-(Ti<sub>3</sub>C<sub>2</sub>@CoO) cathodes and 0.25 M electrolyte (3 mAh g<sup>-1</sup>). These results indicate that electrochemical performance of MSBs can be improved by applying high concentration electrolytes ascribed to less dissolution of magnesium polysulfide in electrolytes. Moreover, this study also demonstrates that MXene-based materials can be a good choice as sulfur host materials for MSBs, expanding a new researching area.

#### Declaration of Competing Interest

The authors declare that they have no known competing financial interests or personal relationships that could have appeared to influence

the work reported in this paper.

#### Acknowledgments

This work was supported by the National Natural Science Foundation of China (No. 51771112), the Science and Technology Commission of Shanghai Municipality (CN) under No. 19511108100, Shanghai Education Commission “Shuguang” scholar project (No. CN, 16SG08) and the funding from Center of Hydrogen Science, Shanghai Jiao Tong University, China. The authors thank Tian Xie for DFT calculations and Dr. Chong Lu for TEM analyses.

#### Appendix A. Supplementary data

Supplementary data to this article can be found online at <https://doi.org/10.1016/j.cej.2021.131031>.

#### References

- [1] J. Muldoon, C.B. Bucur, A.G. Oliver, T. Sugimoto, M. Matsui, H.S. Kim, G.D. Allred, J. Zajicek, Y. Kotani, Electrolyte roadblocks to a magnesium rechargeable battery, *Energy Environ. Sci.* 5 (3) (2012) 5941, <https://doi.org/10.1039/c2ee03029b>.



- [2] M. Mao, T. Gao, S. Hou, C. Wang, A critical review of cathodes for rechargeable Mg batteries, *Chem. Soc. Rev.* 47 (23) (2018) 8804–8841, <https://doi.org/10.1039/C8CS00319J>.
- [3] M. Matsui, Study on electrochemically deposited Mg metal, *J. Power Sources* 196 (16) (2011) 7048–7055, <https://doi.org/10.1016/j.jpowsour.2010.11.141>.
- [4] D.-T. Nguyen, A.Y.S. Eng, M.-F. Ng, V. Kumar, Z. Sofer, A.D. Handoko, G. S. Subramanian, Z.W. Seh, A High-Performance Magnesium Triflate-based Electrolyte for Rechargeable Magnesium Batteries, *Cell Reports Physical Science* 1 (12) (2020) 100265, <https://doi.org/10.1016/j.xcrp.2020.100265>.
- [5] J. Muldoon, C.B. Bucur, T. Gregory, Quest for Nonaqueous Multivalent Secondary Batteries: Magnesium and Beyond, *Chem. Rev.* 114 (23) (2014) 11683–11720, <https://doi.org/10.1021/cr500049y>.
- [6] D. Aurbach, Z. Lu, A. Schechter, Y. Gofer, H. Gizbar, R. Turgeman, Y. Cohen, M. Moshkovich, E. Levi, Prototype systems for rechargeable magnesium batteries, *Nature* 407 (6805) (2000) 724–727, <https://doi.org/10.1038/35037553>.
- [7] J. Song, E. Sahadeo, M. Noked, S.B. Lee, Mapping the Challenges of Magnesium Battery, *J. Phys. Chem. Lett.* 7 (9) (2016) 1736–1749, <https://doi.org/10.1021/acs.jpclett.6b00384>.
- [8] P. Canepa, G. Sai Gautam, D.C. Hannah, R. Malik, M. Liu, K.G. Gallagher, K. A. Persson, G. Ceder, Odyssey of Multivalent Cathode Materials: Open Questions and Future Challenges, *Chem. Rev.* 117 (5) (2017) 4287–4341, <https://doi.org/10.1021/acs.chemrev.6b00614>.
- [9] E. Levi, Y. Gofer, D. Aurbach, On the Way to Rechargeable Mg Batteries The Challenge of New Cathode Materials, *Chem. Mater.* 22 (3) (2010) 860–868, <https://doi.org/10.1021/cm9016497>.
- [10] R. Zhang, X. Yu, K.-W. Nam, C. Ling, T.S. Arthur, W. Song, A.M. Knapp, S. N. Ehrlich, X.-Q. Yang, M. Matsui,  $\alpha$ -MnO<sub>2</sub> as a cathode material for rechargeable Mg batteries, *Electrochem. Commun.* 23 (2012) 110–113, <https://doi.org/10.1016/j.elecom.2012.07.021>.
- [11] Y. Wang, X. Xue, P. Liu, C. Wang, X.u. Yi, Y.i. Hu, L. Ma, G. Zhu, R. Chen, T. Chen, J. Ma, J. Liu, Z. Jin, Atomic Substitution Enabled Synthesis of Vacancy-Rich Two-Dimensional Black TiO<sub>2-x</sub> Nanoflakes for High-Performance Rechargeable Magnesium Batteries, *ACS Nano* 12 (12) (2018) 12492–12502, <https://doi.org/10.1021/acsnano.8b06917>.
- [12] M.D. Regulacio, D.-T. Nguyen, R. Horia, Z.W. Seh, Designing Nanostructured Metal Chalcogenides as Cathode Materials for Rechargeable Magnesium Batteries, *Small* 17 (25) (2021) 2007683, <https://doi.org/10.1002/sml.v17.2510.1002/sml.202007683>.
- [13] L. Chen, J.L. Bao, X. Dong, D.G. Truhlar, Y. Wang, C. Wang, Y. Xia, Aqueous Mg-Ion Battery Based on Polyimide Anode and Prussian Blue Cathode, *ACS Energy Lett.* 2 (5) (2017) 1115–1121, <https://doi.org/10.1021/acseenergylett.7b00040>.
- [14] Y. Shen, Y. Wang, Y. Miao, M. Yang, X. Zhao, X. Shen, High-Energy Interlayer-Expanded Copper Sulfide Cathode Material in Non-Corrosive Electrolyte for Rechargeable Magnesium Batteries, *Adv. Mater.* 32 (4) (2020) 1905524, <https://doi.org/10.1002/adma.v32.410.1002/adma.201905524>.
- [15] D.-T. Nguyen, R. Horia, A.Y.S. Eng, S.-W. Song, Z.W. Seh, Material design strategies to improve the performance of rechargeable magnesium-sulfur batteries, *Mater. Horizons* 8 (3) (2021) 830–853, <https://doi.org/10.1039/D0MH01403F>.
- [16] X. Zhou, J. Tian, J. Hu, C. Li, High Rate Magnesium-Sulfur Battery with Improved Cyclability Based on Metal-Organic Framework Derivative Carbon Host, *Adv. Mater.* 30 (7) (2018) 1704166, <https://doi.org/10.1002/adma.201704166>.
- [17] H.S. Kim, T.S. Arthur, G.D. Allred, J. Zajicek, J.G. Newman, A.E. Rodnyansky, A. G. Oliver, W.C. Boggess, J. Muldoon, Structure and compatibility of a magnesium electrolyte with a sulfur cathode, *Nat. Commun.* 2 (2011) 427, <https://doi.org/10.1038/ncomms1435>.
- [18] Z. Zhao-Karger, X. Zhao, D.i. Wang, T. Diemant, R.J. Behm, M. Fichtner, Performance Improvement of Magnesium Sulfur Batteries with Modified Non-Nucleophilic Electrolytes, *Adv. Energy Mater.* 5 (3) (2015) 1401155, <https://doi.org/10.1002/aenm.201401155>.
- [19] Z. Zhao-Karger, M.E. Gil Bardaji, O. Fuhr, M. Fichtner, A new class of non-corrosive, highly efficient electrolytes for rechargeable magnesium batteries, *J. Mater. Chem. A* 5 (22) (2017) 10815–10820, <https://doi.org/10.1039/C7TA02237A>.
- [20] D.W. Li, S. Cheng, J. Wang, Y. Qiu, Z. Zheng, H. Lin, S. Nanda, Q. Ma, Y. Xu, F. Ye, M. Liu, L. Zhou, Y. Zhang, Synthesis, Crystal Structure, and Electrochemical Properties of a Simple Magnesium Electrolyte for Magnesium Sulfur Batteries, *Angew. Chem. Int. Ed.* 55 (2016) 6406–6410, <https://doi.org/10.1002/anie.201600256>.
- [21] S.-Y. Ha, Y.-W. Lee, S.W. Woo, B. Koo, J.-S. Kim, J. Cho, K.T. Lee, N.-S. Choi, Magnesium(II) bis(trifluoromethane sulfonyl) imide-based electrolytes with wide electrochemical windows for rechargeable magnesium batteries, *ACS Appl. Mater. Interfaces* 6 (6) (2014) 4063–4073, <https://doi.org/10.1021/am405619v>.
- [22] T. Gao, S. Hou, F. Wang, Z. Ma, X. Li, K. Xu, C. Wang, Reversible S<sub>0</sub>/MgS<sub>x</sub> Redox Chemistry in a MgTFSI<sub>2</sub>/MgCl<sub>2</sub>/DME Electrolyte for Rechargeable Mg Batteries, *Angew. Chem. Int. Ed.* 56 (43) (2017) 13526–13530, <https://doi.org/10.1002/anie.v56.4310.1002/anie.201708241>.
- [23] X. Li, T. Gao, F. Han, Z. Ma, X. Fan, S. Hou, N. Eidson, W. Li, C. Wang, Reducing Mg Anode Overpotential via Ion Conductive Surface Layer Formation by Iodine Additive, *Adv. Energy Mater.* 8 (7) (2018) 1701728, <https://doi.org/10.1002/aenm.v8.710.1002/aenm.201701728>.
- [24] K.A. See, K.W. Chapman, L. Zhu, K.M. Wiaderek, O.J. Borkiewicz, C.J. Barile, P. J. Chupas, A.A. Gewirth, The Interplay of Al and Mg Speciation in Advanced Mg Battery Electrolyte Solutions, *J. Am. Chem. Soc.* 138 (1) (2016) 328–337, <https://doi.org/10.1021/jacs.5b10987>.
- [25] C.J. Barile, R.G. Nuzzo, A.A. Gewirth, Exploring Salt and Solvent Effects in Chloride-Based Electrolytes for Magnesium Electrodeposition and Dissolution, *J. Phys. Chem. C* 119 (24) (2015) 13524–13534, <https://doi.org/10.1021/acs.jpcc.5b03508>.
- [26] H. Tian, T. Gao, X. Li, X. Wang, C. Luo, X. Fan, C. Yang, L. Suo, Z. Ma, W. Han, C. Wang, High power rechargeable magnesium/iodine battery chemistry, *Nat. Commun.* 8 (2017) 14083, <https://doi.org/10.1038/ncomms14083>.
- [27] C. Jin, F.A. Rasmussen, K.S. Thygesen, Tuning the Schottky Barrier at the Graphene/MoS<sub>2</sub> Interface by Electron Doping: Density Functional Theory and Many-Body Calculations, *J. Phys. Chem. C* 119 (34) (2015) 19928–19933, <https://doi.org/10.1021/acs.jpcc.5b05580>.
- [28] T. Gao, M. Noked, A.J. Pearce, E. Gillette, X. Fan, Y. Zhu, C. Luo, L. Suo, M. A. Schroeder, K. Xu, S.B. Lee, G.W. Rubloff, C. Wang, Enhancing the reversibility of Mg/S battery chemistry through Li<sup>+</sup> mediation, *J. Am. Chem. Soc.* 137 (38) (2015) 12388–12393, <https://doi.org/10.1021/jacs.5b07820>.
- [29] W. Wang, H. Yuan, Y. NuLi, J. Zhou, J. Yang, J. Wang, Sulfur/microporous Carbon Cathode with a High Sulfur Content for Magnesium-Sulfur Batteries with Nucleophilic Electrolytes, *J. Phys. Chem. C* 122 (46) (2018) 26764–26776, <https://doi.org/10.1021/acs.jpcc.8b09003>.
- [30] H. Fan, Z. Zheng, L. Zhao, W. Li, J. Wang, M. Dai, Y. Zhao, J. Xiao, G. Wang, X. Ding, H. Xiao, J. Li, Y. Wu, Y. Zhang, Extending Cycle Life of Mg/S Battery by Activation of Mg Anode/Electrolyte Interface through an LiCl-Assisted MgCl<sub>2</sub> Solubilization Mechanism, *Adv. Funct. Mater.* 30 (9) (2020) 1909370, <https://doi.org/10.1002/adfm.v30.910.1002/adfm.201909370>.
- [31] X. Liang, A. Garsuch, L.F. Nazar, Sulfur cathodes based on conductive MXene nanosheets for high-performance lithium-sulfur batteries, *Angew. Chem. Int. Ed.* 54 (13) (2015) 3907–3911, <https://doi.org/10.1002/anie.201410174>.
- [32] W. Li, S. Cheng, J. Wang, Y. Qiu, Z. Zheng, H. Lin, S. Nanda, Q. Ma, Y. Xu, F. Ye, M. Liu, L. Zhou, Y. Zhang, Synthesis, Crystal Structure, and Electrochemical Properties of a Simple Magnesium Electrolyte for Magnesium Sulfur Batteries, *Angew. Chem. Int. Ed.* 55 (2016) 6406–6410, <https://doi.org/10.1002/anie.201600256>.
- [33] X. Yu, A. Manthiram, Performance Enhancement and Mechanistic Studies of Magnesium-Sulfur Cells with an Advanced Cathode Structure, *ACS Energy Lett.* 1 (2) (2016) 431–437, <https://doi.org/10.1021/acseenergylett.6b00213>.
- [34] M. Naeubi, M. Kurtoglu, V. Presser, J. Lu, J. Niu, M. Heon, L. Hultman, Y. Gogotsi, M.W. Barsoum, Two-dimensional nanocrystals produced by exfoliation of Ti<sub>3</sub>AlC<sub>2</sub>, *Adv. Mater.* 23 (37) (2011) 4248–4253, <https://doi.org/10.1002/adma.201102306>.
- [35] H. Xu, W. Zhu, F. Sun, H.u. Qi, J. Zou, R. Laine, W. Ding, Turning Trash into Treasure: MXene with Intrinsic LiF Solid Electrolyte Interfaces Performs Better and Better during Battery Cycling, *Adv. Mater. Technol.* 6 (3) (2021) 2000882, <https://doi.org/10.1002/admt.v6.310.1002/admt.202000882>.
- [36] A. Byeon, M.-Q. Zhao, C.E. Ren, J. Halim, S. Kota, P. Urbankowski, B. Anasori, M. W. Barsoum, Y. Gogotsi, Two-Dimensional Titanium Carbide MXene As a Cathode Material for Hybrid Magnesium/Lithium-Ion Batteries, *ACS Appl. Mater. Interfaces* 9 (5) (2017) 4296–4300, <https://doi.org/10.1021/acsaami.6b04198>.
- [37] M. Xu, S. Lei, J. Qi, Q. Dou, L. Liu, Y. Lu, Q. Huang, S. Shi, X. Yan, Opening Magnesium Storage Capability of Two-Dimensional MXene by Intercalation of Cationic Surfactant, *ACS Nano* 12 (4) (2018) 3733–3740, <https://doi.org/10.1021/acsnano.8b00959>.
- [38] F. Liu, Y. Liu, X. Zhao, K. Liu, H. Yin, L.-Z. Fan, Prelithiated V<sub>2</sub>C MXene: A High-Performance Electrode for Hybrid Magnesium/Lithium-Ion Batteries by Ion Intercalation, *Small* 16 (8) (2020) 1906076, <https://doi.org/10.1002/sml.v16.810.1002/sml.201906076>.
- [39] K. Hantanasirisakul, Y. Gogotsi, Electronic and Optical Properties of 2D Transition Metal Carbides and Nitrides (MXenes), *Adv. Mater.* 30 (52) (2018) 1804779, <https://doi.org/10.1002/adma.v30.5210.1002/adma.201804779>.
- [40] S. Zhang, N. Zhong, X. Zhou, M. Zhang, X. Huang, X. Yang, R. Meng, X. Liang, Comprehensive Design of the High-Sulfur-Loading Li-S Battery Based on MXene Nanosheets, *Nano-Micro Lett.* 12 (1) (2020), <https://doi.org/10.1007/s40820-020-00449-7>.
- [41] S. Wu, Y. Wang, S. Na, C. Chen, T. Yu, H. Wang, H. Zhang, Porous hollow carbon nanospheres embedded with well-dispersed cobalt monoxide nanocrystals as effective polysulfide reservoirs for high-rate and long-cycle lithium-sulfur batteries, *J. Mater. Chem. A* 5 (33) (2017) 17352–17359, <https://doi.org/10.1039/C7TA05120D>.
- [42] N. Wang, B. Chen, K. Qin, E. Liu, C. Shi, C. He, N. Zhao, Rational design of Co<sub>9</sub>S<sub>8</sub>/CoO heterostructures with well-defined interfaces for lithium sulfur batteries: A study of synergistic adsorption-electrocatalysis function, *Nano Energy* 60 (2019) 332–339, <https://doi.org/10.1016/j.nanoen.2019.03.060>.
- [43] G. Kresse, D. Joubert, From ultrasoft pseudopotentials to the projector augmented-wave method, *Phys. Rev. B* 59 (3) (1999) 1758–1775, <https://doi.org/10.1103/PhysRevB.59.1758>.
- [44] J.P. Perdew, K. Burke, M. Ernzerhof, Generalized Gradient Approximation Made Simple, *Phys. Rev. Lett.* 77 (18) (1996) 3865–3868, <https://doi.org/10.1103/PhysRevLett.77.3865>.
- [45] M. Ghidui, M.R. Lukatskaya, M.-Q. Zhao, Y. Gogotsi, M.W. Barsoum, Conductive two-dimensional titanium carbide 'clay' with high volumetric capacitance, *Nature* 516 (7529) (2014) 78–81, <https://doi.org/10.1038/nature13970>.
- [46] Z. Li, L. Wang, D. Sun, Y. Zhang, B. Liu, Q. Hu, A. Zhou, Synthesis and thermal stability of two-dimensional carbide MXene Ti<sub>3</sub>C<sub>2</sub>, *Mater. Sci. Eng. B* 191 (2015) 33–40, <https://doi.org/10.1016/j.mseb.2014.10.009>.

- [47] P. Vialat, C. Mousty, C. Taviot-Gueho, G. Renaudin, H. Martinez, J.-C. Dupin, E. Elkaim, F. Leroux, High-Performing Monometallic Cobalt Layered Double Hydroxide Supercapacitor with Defined Local Structure, *Adv. Funct. Mater.* 24 (30) (2014) 4831–4842, <https://doi.org/10.1002/adfm.v24.3010.1002/adfm.201400310>.
- [48] X. Fan, R.R. Gaddam, N.A. Kumar, X.S. Zhao, A Hybrid  $\text{Mg}^{2+}/\text{Li}^{+}$  Battery Based on Interlayer-Expanded  $\text{MoS}_2$ /Graphene Cathode, *Adv. Energy Mater.* 7 (19) (2017) 1700317, <https://doi.org/10.1002/aenm.201700317>.
- [49] Å. Rinnan, F.V.D. Berg, S.B. Engelsen, Review of the most common pre-processing techniques for near-infrared spectra, *Trends Anal. Chem.* 28 (10) (2009) 1201–1222, <https://doi.org/10.1016/j.trac.2009.07.007>.
- [50] K. Tang, A. Du, X. Du, S. Dong, C. Lu, Z. Cui, L. Li, G. Ding, F. Chen, X. Zhou, G. Cui, A Novel Regulation Strategy of Solid Electrolyte Interphase Based on Anion-Solvent Coordination for Magnesium Metal Anode, *Small* 16 (49) (2020) 2005424, <https://doi.org/10.1002/smll.v16.4910.1002/smll.202005424>.
- [51] Y. He, Q. Li, L. Yang, C. Yang, D. Xu, Electrochemical-Conditioning-Free and Water-Resistant Hybrid  $\text{AlCl}_3/\text{MgCl}_2/\text{Mg}(\text{TFSI})_2$  Electrolytes for Rechargeable Magnesium Batteries, *Angew. Chem. Int. Ed.* 58 (2019) 7615–7619, <https://doi.org/10.1002/anie.2018128>.
- [52] Y.V. Mikhaylik, J.R. Akridge, Polysulfide Shuttle Study in the Li/S Battery System, *J. Electrochem. Soc.* 151 (2004) A1969–A1976, <https://doi.org/10.1149/1.1806394>.
- [53] B.P. Vinayan, Z. Zhao-Karger, T. Diemant, V.S.K. Chakravadhanula, N. I. Schwarzburger, M.A. Cambaz, R.J. Behm, C. Kübel, M. Fichtner, Performance study of magnesium-sulfur battery using a graphene based sulfur composite cathode electrode and a non-nucleophilic Mg electrolyte, *Nanoscale* 8 (6) (2016) 3296–3306, <https://doi.org/10.1039/C5NR04383B>.
- [54] N.a. Wu, Y.-C. Lyu, R.-J. Xiao, X. Yu, Y.-X. Yin, X.-Q. Yang, H. Li, L. Gu, Y.-G. Guo, A highly reversible, low-strain Mg-ion insertion anode material for rechargeable Mg-ion batteries, *NPG Asia Mater.* 6 (8) (2014) e120–e121, <https://doi.org/10.1038/am.2014.61>.
- [55] J. Häcker, C. Danner, B. Sievert, I. Biswas, Z. Zhao-Karger, N. Wagner, K. A. Friedrich, Investigation of Magnesium-Sulfur Batteries using Electrochemical Impedance Spectroscopy, *Electrochim. Acta* 338 (2020) 135787, <https://doi.org/10.1016/j.electacta.2020.135787>.
- [56] Q. Zhao, R. Wang, Y. Zhang, G. Huang, B. Jiang, C. Xu, F. Pan, The design of  $\text{Co}_3\text{S}_4$ @MXene heterostructure as sulfur host to promote the electrochemical kinetics for reversible magnesium-sulfur batteries, *J. Magnes. Alloy.* 9 (1) (2021) 78–89, <https://doi.org/10.1016/j.jma.2020.12.001>.
- [57] K.R.G. Lim, A.D. Handoko, S.K. Nemani, B. Wyatt, H.-Y. Jiang, J. Tang, B. Anasori, Z.W. Seh, Rational Design of Two-Dimensional Transition Metal Carbide/Nitride (MXene) Hybrids and Nanocomposites for Catalytic Energy Storage and Conversion, *ACS Nano* 14 (9) (2020) 10834–10864, <https://doi.org/10.1021/acsnano.0c05482>.
- [58] A.D. Handoko, H. Chen, Y. Lum, Q. Zhang, B. Anasori, Z.W. Seh, Dimensional Titanium and Molybdenum Carbide MXenes as Electrocatalysts for  $\text{CO}_2$  Reduction, *iScience* 23 (6) (2020) 101181, <https://doi.org/10.1016/j.isci.2020.101181>.
- [59] A.D. Handoko, K.D. Fredrickson, B. Anasori, K.W. Convey, L.R. Johnson, Y. Gogotsi, A. Vojvodic, Z.W. Seh, Tuning the Basal Plane Functionalization of Two-Dimensional Metal Carbides (MXenes) To Control Hydrogen Evolution Activity, *ACS Appl. Energy Mater.* 1 (1) (2018) 173–180, <https://doi.org/10.1021/acsaem.7b00054>.